

Bridging-Controlled Network Microstructure and Long-Wavelength Fluctuations in Silica–Poly(2-vinylpyridine) Nanocomposites: Experimental Results and Theoretical Analysis

Yuxing Zhou, Benjamin M. Yavitt, Zhengping Zhou, Vera Bocharova, Daniel Salatto, Maya K. Endoh, Alexander E. Ribbe, Alexei P. Sokolov, Tadanori Koga, and Kenneth S. Schweizer*

Cite This: *Macromolecules* 2020, 53, 6984–6994

Read Online

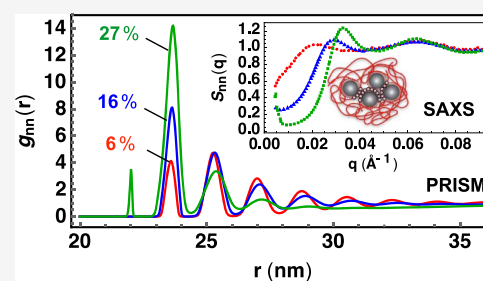
ACCESS |

Metrics & More

Article Recommendations

Supporting Information

ABSTRACT: We have performed small-angle X-ray scattering (SAXS) measurements to study the evolution of length-scale-dependent nanoparticle (NP) correlations over a wide range of loadings in miscible silica–poly(2-vinylpyridine) polymer nanocomposites (PNC) characterized by strong interfacial attraction. The local cage and intermediate-scale correlations evolve in a commonly observed manner with increasing silica concentration, while long-wavelength concentration fluctuations exhibit a complex behavior. Higher-loading PNCs show a non-monotonic change in the structure factor amplitude with wavevector because of an upturn on the longest length scales, which is the most intense for the highest NP concentration sample. These observations suggest that the PNC is approaching a spinodal demixing transition of an unusual polymer bridging-induced network type. PRISM integral equation theory is quantitatively applied, captures the key features of the SAXS data, and provides a theoretical basis for a network-like phase separation analogous to polyelectrolyte coacervation. The theory with validated parameters is then used to make predictions of real-space pair correlation functions between all species, the small- and large-wavevector collective polymer structure factor, spatially resolved NP coordination numbers, the interfacial cohesive energy density, and a measure of an enlarged effective NP radius because of polymer adsorption. With increasing NP loading, intensification of tight secondary bridged NP configurations, but weakening of interpolymer and polymer–NP correlations due to packing frustration, is predicted. This local reorganization of the polymer structure coexists with macro- and microphase separation such as features at low wavevectors which vary distinctively with NP loading. The predictions for the collective polymer structure are potentially testable using scattering experiments. Our results provide an important starting point for building an understanding of collective NP dynamics.

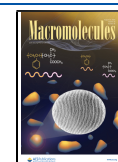


1. INTRODUCTION

Polymer nanocomposites (PNCs) continue to be of significant fundamental scientific and applied interest given their rich array of structural, dynamical, and mechanical behaviors that involve both polymer and colloid science aspects.^{1–3} Many experimental studies exist for how nanoparticles (NPs) change PNC bulk mechanical properties, polymer center-of-mass diffusion, polymer segmental dynamics, T_g , and rheology.^{1–5} A strong recent focus has been on the nature of perturbed polymer static and dynamic layers near a NP surface in the melt.^{3,6–16} On the other hand, the number of comprehensive studies of the length-scale-dependent mixture microstructural pair correlations is more limited, and determination of equilibrium phase diagrams is even more rare. One reason is the difficulty of separately probing the polymer and NP structural correlations over a wide range of length scales with scattering or microscopy methods. Another issue is whether the presence of relatively strong interfacial attractions, generally required to disperse NPs and avoid macroscopic phase separation, results in nonequilibrium effects and/or gelation.

In contrast, there has been significant simulation and theoretical work on model PNCs.^{17–26} The most advanced and well-developed theoretical approach for the equilibrium structure and phase behavior is polymer reference interaction site model (PRISM) integral equation theory.^{21,27–29} The states of the organization map and phase separation boundaries have been determined based on a minimal model, as schematically indicated in Figure 1. At very low polymer–NP attraction strength, the PNC experiences entropic depletion interactions which drive NPs to contact cluster and ultimately phase separate into nearly pure polymer and NP phases. As the interfacial attraction becomes of the order of the thermal energy $k_B T$, discrete adsorbed polymer layers form,

Received: June 15, 2020
 Revised: July 24, 2020
 Published: August 12, 2020



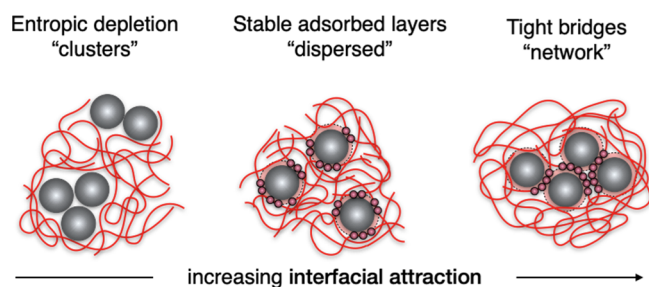


Figure 1. States of organization predicted by PRISM theory with increasing interfacial attraction.^{20,21} Phase separation occurs at low and high enough strengths of attraction. Only the tightest bridging configuration is shown, while in practice, secondary or tertiary bridging configurations can be very important corresponding to two or three layers of polymer segments bridging two NP surfaces.

which can induce an effective steric stabilization and a net repulsive potential of mean force (PMF) between NPs, resulting in good dispersion. This opens a window of miscibility in dimensionless strength of attraction-NP loading space, the details of which depend on mixture total packing fraction, NP size and degree of loading, range of interfacial attraction, and to a much lesser degree polymer chain length and backbone stiffness. At large enough interfacial attraction, the discrete adsorbed polymer layers become thermodynamically disfavored, and relatively *tight* polymer-mediated bridges between NPs are predicted to emerge driven by enthalpic considerations, resulting in a network-like microstructure. A common motif of the latter is a cohesive bridging configuration where NPs are separated by 1–3 layers of polymer chain segments (tight, secondary, and tertiary) depending on the range and strength of attraction and NP loading. PRISM theory predicts that this change of the microstructure can ultimately result in enthalpy-driven phase separation of a qualitatively different nature than depletion-driven demixing. Moreover, total density fluctuations (mixture compressibility) play an important role and the coexisting phases consist of a dense polymer–NP network in equilibrium with a dilute phase. This type of phase separation is analogous to the so-called coacervation in mixtures of oppositely charged polymers.^{30,31} The basic predictions of PRISM theory for the polymer-mediated NP PMF and phase behavior have been largely confirmed, at least qualitatively, by simulations of coarse-grained models.^{17,23}

Experimentally, Zukoski and co-workers^{32–34} have performed multiple small-angle X-ray scattering (SAXS) measurements of NP collective structure factors over a wide range of loadings for PNCs with short-chain polymers that attract NPs via moderate strengths. The theoretical prediction of a transition between depletion-driven NP clustering to a sterically stabilized homogeneous PNC phase with discrete adsorbed layers has been largely confirmed for silica NPs in poly(ethylene oxide) and poly(tetrahydrofuran) melts and dense solutions.³² Quantitative confrontations of PRISM theory predictions of the collective NP scattering structure factors over a wide range of wavevectors have been performed.³³ Generally good agreement between the theory and experiment has been demonstrated for equilibrated PNCs based on adjusting a single-key chemical parameter—the *effective* segmental NP adsorption energy (as per Figure 1). One neutron-scattering study³⁴ employed selective deuterium labeling to measure all three partial collective structure factors

(polymer–polymer, polymer–NP, and NP–NP) over a wide range of loadings. PRISM theory was shown to capture the full microstructural correlations very well-based on the single interfacial attraction energy model.

However, to date, there does not appear to be any systematic SAXS studies of the NP collective structure and phase behavior for PNCs that experience very strong interfacial attractions where bridging and network formation should be dominant. Experimental scattering or structural evidence for the bridging-induced demixing transition does not appear to exist. This is the primary topic of the present article—a combined experimental and theoretical study of silica–poly(2-vinyl pyridine) (P2VP) PNCs where the interfacial attraction is due to strong hydrogen bonding. This system has been a prototypical model system of “well-dispersed” globally homogeneous PNCs, although bridging-mediated attraction must be present given the rheological observations of gel formation and NP organization deduced using electron microscopy.^{3,35} Our new experimental scattering data find evidence for the emergence of significant long-wavelength concentration fluctuations consistent with this PNC approaching a network bridging type of phase transition, as predicted by PRISM theory. These scattering data are quantitatively analyzed with PRISM theory which provides an estimate of the *effective* segmental adsorption energy, and good agreement between theory and SAXS measurements for key features is demonstrated.

The validated theory is then used as a tool to study the real-space NP structure, NP local coordination numbers, interfacial cohesive energy density (CED), NP effective radius, and polymer–polymer and polymer–NP correlation functions in the real and Fourier space. Most of these properties are not accessible experimentally. The theoretical results facilitate construction of a real-space physical picture of the nm-scale microstructure. These results are of intrinsic interest and are also relevant to our future combined experimental–theoretical studies of NP collective dynamics.

In Section 2, we present our experimental approach and SAXS and transmission electron microscopy (TEM) data. Section 3 briefly reviews PRISM theory, and Section 4 uses it to analyze the NP structure factor data. The theory is then employed in Sections 5 and 6 to study the many other quantities and questions mentioned above. The article concludes with a brief discussion in Section 7. The Supporting Information includes additional experimental data and additional theoretical calculations relevant to our analysis.

2. EXPERIMENTAL NP COLLECTIVE SCATTERING AND MICROSTRUCTURE

2.1. Methods and Details. Silica (SiO₂) NPs were synthesized in ethanol according to the Stöber method.^{36,37} The silica–ethanol solution was passed through a 0.2 μm PTFE filter to remove any aggregates and dust. The NPs have an average radius of $R = 9.1$ nm and a size dispersity of 18.3%. The NP density is $\rho = 2.406$ g/cm³.³⁸ P2VP (melt density is $\rho = 1.194$ g/cm³) was purchased from Scientific Polymer Products Inc. The molecular weight is $M_n = 38$ kg/mol and polydispersity index is 1.1.

SiO₂–P2VP PNCs were prepared by dissolving polymer and NPs in an ethanol solution at various NP volume fractions (η_n) of 0.01, 0.06, 0.16, and 0.27. Solutions were drop cast into Teflon dishes followed by evaporation of ethanol over 24–36 h. Excess solvent was removed in a drying vacuum at $T = 120$

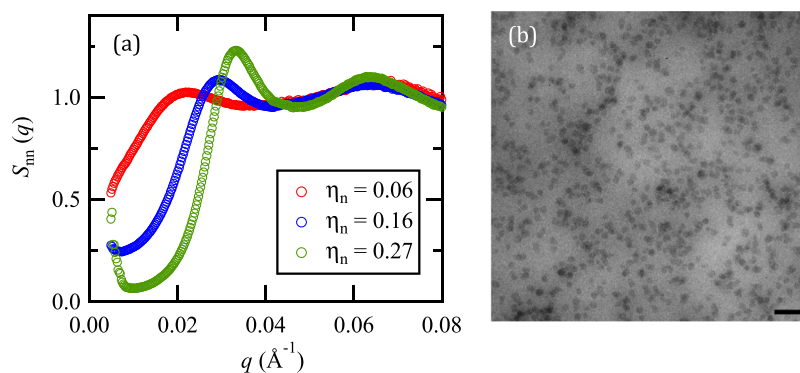


Figure 2. (a) Structure factor $S_{nn}(q)$ obtained from the SAXS measurements for $\eta_n = 0.06, 0.16,$ and 0.27 at $T = 180$ °C. (b) TEM image of the PNC sample with $\eta_n = 0.06$. The scale bar corresponds to 100 nm.

°C for 3 days. The dried bulk PNC flakes were collected from the Teflon dish and the final NP composition was determined by thermogravimetric analysis (TGA). The NP volume (or packing) fraction, η_n , was subsequently calculated using the reported densities. Samples were prepared for $\eta_n = 0.01, 0.06, 0.16,$ and 0.27 . For scattering experiments, PNC flakes were loaded into metal washers (thickness ranging from 0.5 to 2 mm) backed with 50 μm thick polyimide tape (Caplinq) and placed in a vacuum oven for thermal annealing and removal of excess air bubbles. Samples were heated at $T = 180$ °C, which is below the thermal degradation temperature (200 °C),³⁹ for 12 h to remove air bubbles that were introduced during sample preparation, followed by subsequent cooling to room temperature (with an average cooling rate of 4 °C/min).

SAXS measurements were conducted at Beamline 11-BM (Complex Material Scattering) of National Synchrotron Light Source-II (NSLS-II, Brookhaven National Laboratory). Pre-annealed samples were placed on a thermal heating stage in transmission orientation. Samples were heated from room temperature ($T = 25$ °C) to $T = 150$ °C followed by a series of temperature increases at 10 °C intervals up to $T = 190$ °C with an equilibration time of 10 min at each temperature before the measurements. The SAXS data were collected on a Dectris 2M detector (pixel size = 75 $\mu\text{m} \times 75 \mu\text{m}$) at a sample-to-detector distance of 2 m, using an X-ray beam with an energy of 13.5 keV (the corresponding wavelength $\lambda = 0.92$ Å) and exposure time of 15 s. All scattering intensities $I(q)$ were corrected for sample transmission and background scattering.

Sample preparation for transmission electron microscopy (TEM) was done using room temperature ultramicrotomy (Leica UCT) and freshly prepared glass knives. Composite films were microtomed at a thickness of 50 nm and placed on copper grids with a 2–3 nm carbon support film. Imaging was performed using a JEOL JEM-2200FS energy filtered TEM at an accelerating voltage of 200 kV. All imaging was done utilizing zero-loss filtering with a slit width of 10 eV for providing enhanced contrast while staying close to the focus (–200 nm under focus max).

2.2. Results. SAXS raw intensity spectra, $I(q)$, for $\eta_n = 0.06, 0.16,$ and 0.27 at a temperature of $T = 180$ °C [far above the PNC glass transition temperature ($T_g \sim 102$ °C)]³⁹ are presented in Figure S1 of the Supporting Information. The structure is resolved over an exceptionally wide q range (0.005–0.2 \AA^{-1}), corresponding to dimensionless wavevectors of $qD \sim 0.91$ –36, where $D = 2R \sim 18.2$ nm. This range covers the relatively long length scale regime controlled by NP concentration fluctuations to well beyond the interparticle cage

peak. The presence of the interparticle peaks in $I(q)$ around $q = 0.02$ –0.03 \AA^{-1} for all the PNCs indicates good global NP dispersion. The measured spectra of the dilute sample ($\eta_n = 0.01$) were used to calculate the NP form factor $P(q)$ (Figure S2). The dispersed NPs in the polymer matrix possess an interfacial polymer layer on the NP surface because of the attractive interactions between SiO_2 and P2VP,^{39,40} which is known to have different physical properties compared to the bulk P2VP matrix.^{3,10,38,41} Motivated by these previous results, we fit the SAXS profile at $\eta_n = 0.01$ using a polydisperse core (SiO_2 NP)–shell (the interfacial layer) model. The best fit is shown as a solid line through the experimental $I(q)$ data in Figure S2.⁴² The interfacial layer thickness was estimated to be ~ 3 nm. We also found that the density of the “shell” interfacial layer at $\eta_n = 0.01$ is slightly ($\sim 5\%$) higher than that of the bulk polymer. Overall, the interfacial layer structure is in agreement with previous results on a similar material system.^{9,38}

The NP collective structure factor $S_{nn}(q)$ was then calculated by dividing $I(q)$ by the form factor ($S_{nn}(q) = I(q)/P(q)$). The results are plotted in Figure 2a. The primary peak position (q^*) of $S_{nn}(q)$ is crudely related to a mean interparticle spacing (d), where $d \sim 2\pi/q^*$. However, in reality, there is a broad distribution of NP separations in the locally heterogeneous microstructure because of polymer-mediated NP clustering. An example of this is in Figure 2b, where a TEM image of the PNC sample with $\eta_n = 0.06$ is shown. Globally, the NPs are well-dispersed but local clustering is clearly present. Such a broad distribution of interparticle distances, in conjunction of NP size polydispersity, is reflected in a broad peak in $S_{nn}(q)$ (Figure 2a).

Increasing the NP loading η_n leads to an increase in q^* , indicating the expected decrease in the average interparticle distance d and also narrowing of the cage peak indicative of some modest amount of improved short-range order. However, the peak intensity of the latter remains quite small. The intensity at lower wavevectors quantifies the NP subsystem osmotic compressibility or amplitude of long-wavelength NP concentration fluctuations. In a fully dispersed system, one expects that this quantity will decrease with NP loading. On the other hand, for NPs that attract directly or via polymer-mediated bridging, there can be enhanced heterogeneity with increasing loading which will increase the low wavevector intensity and in principle can lead to a divergence as $q \rightarrow 0$ if the system approaches a spinodal-phase separation boundary. Our data show that the former trend is initially obeyed and strictly followed on mesoscopic but finite length scales. However, on the longest length (lowest wavevector)

scale, the structure factor amplitude is a nonmonotonic function of loading. Moreover, there is a strong upturn of $S_{nn}(q)$ at small q for the sample with $\eta_n = 0.27$, which crosses the curve of $\eta_n = 0.16$ at very low q . A much weaker upturn in $S_{nn}(q)$ at low q is also visible for the sample with $\eta_n = 0.16$. This suggests that the PNC is beginning to develop large long-wavelength concentration fluctuations, indicative of an impending demixing phase transition of some nature. We find no significant temperature dependence of $S_{nn}(q)$ in the studied temperature range (Figure S3).

The remainder of the article is devoted to a statistical mechanical theory analysis of the SiO₂–P2VP PNC. Based on combining experiment and theory for the NP collective structure factor, two key microscopic parameters (PNC effective total packing fraction and interfacial attraction strength) for the SiO₂–P2VP system can be determined and the key features of our scattering observations are understood. We then use the validated theory as a tool to study multiple real-space structural correlations and a thermodynamic property and to make testable predictions for polymer collective scattering patterns.

3. MODEL AND THEORY

We adopt a widely studied *one* effective interfacial attraction energy minimalist model of a PNC.^{20,21,27} Polymers are modeled as hard-sphere tangent bead Koyama semiflexible chains⁴³ with $N = 100$ segments or interaction sites of diameter σ . We emphasize that increasing N has almost no effect on any of our melt PNC results, as is well-known from prior PRISM theory studies.^{21,43,44} The backbone bending energy is chosen to yield a typical homopolymer persistence length, taken here as $4\sigma/3$. NPs are modeled as smooth hard spheres of diameter $D = 2R$. The one-energy scale enters via a short-range attraction between a polymer segment and NP of an exponential form beyond the hard-core distance of the closest approach ($r_c = (D + \sigma)/2$)

$$u_{pn}(r) = -\epsilon_{pn} \exp\left(-\frac{r - r_c}{\alpha\sigma}\right), \quad r \geq r_c \quad (1)$$

where $\alpha = 0.5$ defines the attraction range. The effective attraction strength ϵ_{pn} in units of $k_B T$ is the key chemically specific parameter. Physically, it represents^{21,44} the lowering of the energy associated with a segment being transferred from a pure polymer melt environment (where in reality it experiences cohesion interactions) to in contact with the NP surface. Given this meaning plus our use of coarse-grained polymer and NP models, it is not appropriate to quantitatively compare this effective adsorption energy with that of a single hydrogen bond between an amino and hydroxyl group computed using gas phase quantum chemistry. Experimentally, the mean diameter of bare SiO₂ NPs is $D \sim 18.2$ nm, while the P2VP Kuhn segment diameter is $\sigma \sim 1\text{--}2$ nm, resulting in a size ratio of $D/\sigma \sim 9\text{--}18$. We adopt $D/\sigma = 10$ based on computational cost considerations; modest variations have little effect on our results.

The total packing fraction $\eta_t = \pi(\rho_p\sigma^3 + \rho_n D^3)/6$ is not precisely known experimentally but is tightly constrained for any dense liquid. We explore below whether (a priori *not* assured) choosing a sensible value in conjunction with varying the interfacial attraction energy in units of the thermal energy, $\beta\epsilon_{pn}$, can lead to a consistent description of all the key features of the experimental $S_{nn}(q)$. Such an exercise of combining

theory and SAXS data has been successfully carried out previously for SiO₂ PNCs in hydrocarbon polymer melts, where the chains are very short and the interfacial attraction is relatively weak.³² For simplicity and because of the absence of precise experimental knowledge to calibrate models, we assume that η_t is loading independent. An alternative method with a loading dependent η_t is explored in the SM and does not lead to any significant change in our results.

The well-known coupled mixture PRISM integral equations in Fourier space can be written in a matrix form as^{27,43,45,46}

$$\mathbf{H}(q) = \mathbf{\Omega}(q)\mathbf{C}(q)[\mathbf{\Omega}(q) + \mathbf{H}(q)] \quad (2)$$

where $H_{ij}(q) = \rho_i\rho_j h_{ij}(q)$ is the (dimensional) total site–site correlation function, with $h_{ij}(q)$ the Fourier transform of $h_{ij}(r) = g_{ij}(r) - 1$, $C_{ij}(q)$ is the site–site direct correlation function, and $\Omega_{ij}(q) = (\rho_i + \rho_j)/(1 + \delta_{ij})\omega_{ij}(q)$ is the (dimensional) intramolecular structure factor matrix. For PNCs, the only nonzero intramolecular structure factors are $\omega_{pp}(q)$ for polymers computed using the Koyama model and $\omega_{nn}(q) = 1$ for hard spheres; the subscripts “p” and “n” indicate the polymer and NP, respectively. The dimensional partial collective structure factor matrix is

$$\mathbf{S}^*(q) \equiv \mathbf{\Omega}(q) + \mathbf{H}(q) \quad (3)$$

and the dimensionless analogues are $S_{ij}(q) = (\rho_i\rho_j)^{-1/2}S_{ij}^*(q)$.

The PRISM equations are closed using our recently developed “modified Verlet” (MV) closure approximation applied to *all* three correlation functions,^{47,48}

$$g_{ij}(r) = \exp[-\beta u_{ij}(r) + \gamma_{ij}(r) + b_{ij}^{MV}(r)]$$

$$b_{ij}^{MV}(r) = -\frac{A\gamma_{ij}(r)^2}{1 + B|\gamma_{ij}(r)|} \quad (4)$$

where $\gamma_{ij}(r) \equiv h_{ij}(r) - c_{ij}(r)$ and $A = 1/2$ and $B = 4/5$. This new closure, which we call the “triple MV”, has been shown to be superior to many other closure approximations for strongly size-asymmetric mixtures in the presence and absence of strong interfacial attractions. In ref 48, we presented a detailed computational study using the triple MV closure of the pair correlation functions and phase behavior of a binary sphere (colloidal) mixture with large size asymmetry⁴⁸ and quantitatively confronted the results with both simulation and many other closure approximations. We showed that the triple MV-based predictions agree well in an absolute sense with simulation and are significantly better than all the other (many) closures we tested, including the classic PY–HNC–PY closure (Percus–Yevick (PY) closure for small–small and small–large particle direct correlations and hypernetted chain (HNC) closure for large–large particle direct correlation)^{21,44} often employed for highly size-asymmetric dense-sphere mixtures and PNCs based on PRISM theory. This work⁴⁸ is directly relevant to the present PNC model system because it shows the same states of organization behavior as size asymmetric sphere mixtures (i.e., the three regimes of depletion, steric stabilization, and bridging, as per Figure 1). Hence, we logically expect that the triple MV approximation will be superior to the classic PY–HNC–PY approximation in the context of PRISM theory for PNCs. Preliminary combined PRISM theory and simulation studies of PNCs support this expectation, and the results of this major study will be reported in a future article.

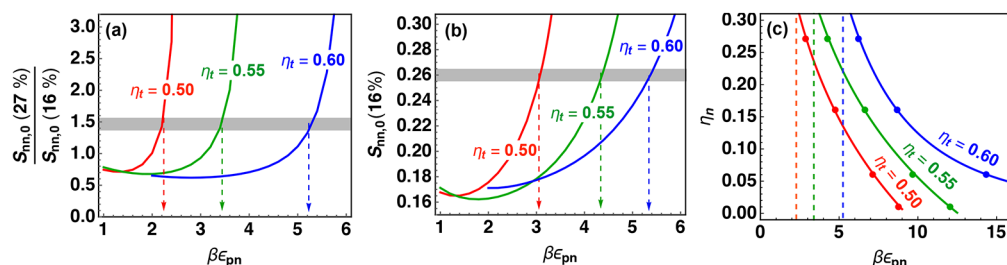


Figure 3. (a) Calculations of the ratio of $S_{nn}(q=0)=S_{nn,0}$ at the two highest loadings and (b) $S_{nn,0}$ at 16% loading as a function of the interfacial attraction for three total PNC packing fractions. Gray bands indicate the estimated experimental values at 180 °C. (c) Bridging spinodal boundaries with the dashed vertical lines indicating $\beta\epsilon_{pn} = 2.2, 3.4,$ and 5.2 for $\eta_t = 0.5, 0.55,$ and $0.6,$ respectively.

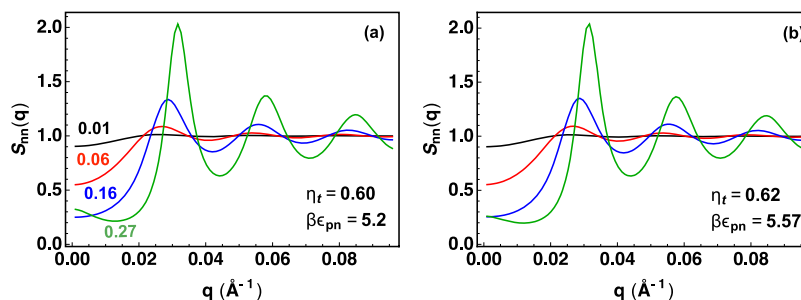


Figure 4. (a) Theoretical $S_{nn}(q)$ with optimized values of η_t and $\beta\epsilon_{pn}$ at 180 °C. (b) Predicted analogues at 150 °C.

4. THEORETICAL ANALYSIS OF NP SCATTERING AND COMPARISON TO THE EXPERIMENT

4.1. Parameter Selection. As per above, the size ratio is taken as $D/\sigma = 10$, and the NPs are monodisperse in size. The NP volume fractions (more accurately called “packing fractions” in liquids) studied are the same as in our experiments: $\eta_n = 0.01, 0.06, 0.16,$ and 0.27 , defined as $\eta_n = \pi\rho_n D^3/6$.

We first recall a few key features of the SAXS measurements (Figure 2a) that frame our theoretical analysis. There are the normal trends of narrowing and blue shift of the cage peak from $q^* \sim 0.021$ to 0.032 \AA^{-1} as η_n increases from 0.06 to 0.27. Most importantly, there is a strong upturn of $S_{nn}(q)$ at small q for $\eta_n = 0.27$, which crosses the $\eta_n = 0.16$ system curve at very low q . This upturn is typically a signature of approaching spinodal phase separation, although the upturn is “weak” in the sense that $S_{nn}(q \sim 0)$ is still below the random value of unity for our system. The magnitude of the cage peak increases with loading, which correlates sensibly with a decreasing amplitude of $S_{nn}(q)$ at lower wavevectors above $q \sim 0.01 \text{ \AA}^{-1}$. We note that the absolute amplitude of the experimental cage peak is modest, perhaps because of a combination of NP polydispersity, a soft NP surface due to adsorbed polymers, and/or the relatively low loading. Furthermore, we also perform calculations for 1% loading to establish a baseline dilute limit behavior where one expects $S_{nn}(q) = 1$ to leading order.

We now explore whether sensible choices of $\beta\epsilon_{pn}$ and η_t allow PRISM theory to capture the *essential* features of the experimental data in Figure 2a. Given the chemical complexity of the silica–P2VP system, our goal is not to fit curves through the data. We consider three total PNC packing fractions that span the range of essentially all dense liquids: $\eta_t = 0.50, 0.55,$ and 0.60 . The effective segmental–NP interfacial dimensionless attraction strength, $\beta\epsilon_{pn}$, is varied from moderate to strong, 1–6. For each fixed η_t , $S_{nn}(q)$ is calculated for $\eta_n = 0.01, 0.06, 0.16,$ and 0.27 . Because the crossing of scattering curves and

upturns of the two highest NP concentration systems at low q is the most important (and certainly most novel) feature that should be captured by the theory, we choose the ratio of $S_{nn}(0)$

between two highest loadings, $Q(\eta_t, \beta\epsilon_{pn}) = \frac{S_{nn,0}(\eta_n = 0.27)}{S_{nn,0}(\eta_n = 0.16)}$,

as the primary metric for calibration of our two model parameters. As shown in Figure 3a, for each η_t studied, one can adjust $\beta\epsilon_{pn}$ such that $Q(\eta_t, \beta\epsilon_{pn})$ matches the experimental value of $Q_{exp} \sim 1.5$. As a second constraint, the predicted absolute value of $S_{nn}(0)$ at $\eta_n = 0.16$ is compared with experiments in Figure 3b. We find that for $\eta_t = 0.6$ and $\beta\epsilon_{pn} \sim 5.2$, both $S_{nn,0}(\eta_n = 0.16)$ and $Q(\eta_t, \beta\epsilon_{pn})$ agree well with experiment, whereas other combinations of η_t and $\beta\epsilon_{pn}$ do not agree as well. We also checked that for $\eta_n = 0.06$, the $S_{nn}(0)$ is relatively insensitive to the precise choice of parameters and agree with experiment.

We emphasize that the theoretical *predictions* of $Q(\eta_t, \beta\epsilon_{pn})$ and $S_{nn,0}(\eta_n = 0.16)$ are *very* sensitive to $\beta\epsilon_{pn}$ for strong attractions, which is important for our calibration approach. The physical reason is related to the system approaching a polymer-mediated bridging spinodal, as illustrated in Figure 3c. Note that the effective attraction energy needed to induce network demixing *decreases* with loading and also with reduction in the total PNC packing fraction because this type of phase separation involves strong compressibility effects. The latter behavior is very different than the classic type of demixing where the two species separate into nearly pure coexisting phases (as per the left image in Figure 1).

4.2. Predictions for Collective NP Structure Factors.

Having calibrated the two parameters that enter our minimalist model using experimental data at a *single* value of (low) wavevector, we compute the full NP structure factors (and many other quantities) using $\eta_t = 0.6$ and $\beta\epsilon_{pn} = 5.2$. Although the latter cannot be compared quantitatively to a gas-phase quantum chemical calculation, its relatively large magnitude ($\sim 19 \text{ kJ/mol}$) is in the range expected for a hydrogen bond and thus seems qualitatively consistent with the specific PNC

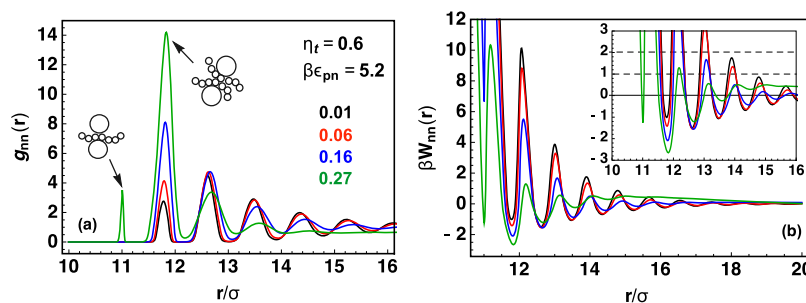


Figure 5. (a) NP–NP pair correlation function as a function of reduced separation at different loadings. (b) Corresponding PMF in thermal energy units. The inset shows an expanded view of local barriers and minima. For reference, the solid horizontal line indicates a PMF of zero. The two dashed horizontal lines indicate when the PMF equals 1 and $2 k_B T$, which defines characteristic NP separations that are discussed below.

studied, which is known to form strong polymer–NP hydrogen bonds.

Figure 4a shows our 180 °C results for $S_{nn}(q)$, which can be compared to the experimental data in Figure 2a. We again emphasize that given the complexity of the experimental system and simplicity of our minimalist model, the aim is not to quantitatively fit the theory to achieve the best agreement with experimental scattering curves over all wavevectors. Rather, we focus on the key features as discussed above. If the reader is interested, see Figure S4 for plots of the experimental data overlaying the theory results in Figure 4.

Figure 4a shows that the theory captures almost quantitatively the main features observed in the experiment that we have emphasized above, that is, a blue shift of the cage peak position $q^* \sim 0.028$ to 0.032 \AA^{-1} with $\eta_n = 0.06$ – 0.27 , the crossing of $S_{nn}(0)$ at two highest loadings at $q \sim 0.005 \text{ \AA}^{-1}$, and the location of the minimum for $\eta_n = 0.27$ at ~ 0.01 – 0.015 \AA^{-1} . Although the theory properly captures the narrowing and growth in the intensity of the cage peak with loading, the predicted amplitude, $S_{nn}(q^*)$, is significantly larger than that found in the experiment. We do not have a good understanding of the origin of this difference but speculate that it may be due to particle size polydispersity which can smear and broaden the cage peak and/or limitations of our coarse-grained modeling of the polymers. At present, we cannot explicitly test this idea because including size polydispersity in PRISM theory of PNCs is an open problem.

Figure 4b shows the analogous theoretical results at 150 °C. Lowering temperature enters via a small increase in the density (and hence total packing fraction) estimated from the known thermal expansion coefficient ($\sim 0.001 \text{ K}^{-1}$) and a small increase in the ratio of the adsorption energy to the thermal energy. This change of temperature has very little consequences on the predicted NP structure factors, consistent with our experimental SAXS data in Figure S3.

4.3. Alternative Analyses. To test the robustness of our modeling and as a crude attempt to mimic constant pressure conditions in size-asymmetric mixtures, we follow prior combined PRISM-SAXS studies³² and consider an adjusted total packing fraction model

$$\eta_t = \eta_{p,0} + \eta_n(1 - \eta_{p,0}(1 + (\sigma/D)^3)) \quad (5)$$

where $\eta_{p,0}$ is the packing fraction of the pure polymer melt and η_n is the NP packing fraction in the PNC. Equation 5 implies that the total mixture packing fraction grows with NP loading as a geometric consequence of smaller polymer segments being able to explore interstitial regions between the larger NPs. Equation 5 was derived based on the assumption that the local

polymer packing fraction *outside* the volume excluded by NPs remains the same as that in the pure melt.³² To implement this model in an illustrative manner, we choose $\eta_{p,0} = 0.50$ and adjust the total PNC packing fraction for each η_n according to eq 5. For $\eta_n = 0.27$, the corresponding $\eta_t = 0.59$ is close to our calculations with a constant $\eta_t = 0.60$. Thus, we expect a similar behavior of the $S_{nn}(0)$ ratio for the two highest loadings based on using the same $\beta\epsilon_{pn} = 5.2$. This expectation is explicitly confirmed in Figure S5.

Finally, we note that the simultaneous presence of an upturn of $S_{nn}(q)$ at low q and a large $S_{nn}(q^*)$ in Figure 4 is a distinct feature of dense binary mixtures approaching demixing. It qualitatively contrasts with taking literally the NP subsystem as an effective hard sphere fluid, as discussed in the Supporting Information and explicitly shown in Figure S6.

5. REAL-SPACE NP STRUCTURE AND PROPERTIES

We now present calculations of the real-space NP correlations and related quantities based on the calibrated constant total packing fraction model of Section 4.

5.1. Real-Space Correlations. Figure 5a shows the real-space NP–NP pair correlation or radial distribution functions $g_{nn}(r)$. Because of the strong polymer–NP attraction, the probability that two NPs are in contact is essentially zero. The locations of the peaks define the mean interparticle surface-to-surface separations of distinct local bridging states. One sees that they occur (as expected) when a pair of NP surfaces is separated by roughly 1, 2, and 3 segment diameters. The evolution of the peak heights as a function of loading η_n reflects changes in the relative probability of the different local bridging states. The tightest or “primary” bridging configuration of two NPs separated by one layer of segments is also very improbable. The secondary bridging peak observed in $g_{nn}(r)$ at $(r - D) \sim 2\sigma$ is comparable in intensity to its tertiary analogue at lower loadings but becomes much more important and intense at higher NP loadings. The question of the relative probabilities of tight, secondary, and tertiary bridging configurations relates to local packing entropy versus local correlated enthalpy considerations, which both depend on NP loading. Another reflection of this competition is that at the highest loading of $\eta_n = 0.27$ and when NP surfaces are the closest, a tight bridging peak emerges, although it is of secondary importance. A rather remarkable generic feature is the *very* sharp nature of the bridging peaks, with $g_{nn}(r)$ in the interstitial region nearly zero, to a degree that is enhanced as NP loading decreases. In addition, the bridging peak amplitudes decay more quickly with NP separation as loading grows, indicating a reduced correlation length of the bridging

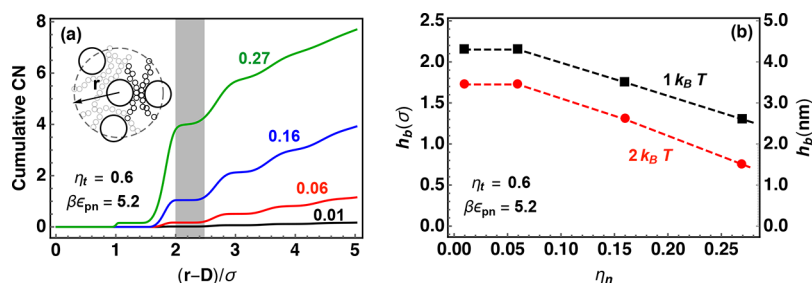


Figure 6. (a) Cumulative coordination number of NPs as a function of surface-to-surface separation for different loadings. The gray-shaded region indicates the most important tight bridging separation of 2 segment diameters. (b) Magnitude of the effective radius enhancement due to polymer adsorption as a function of loading computed from the PMF based on the distance of closest approach of 1 and $2 k_B T$, as per the inset of Figure 5b. Results are shown in units of the segment diameter and in nm based on the choice $\sigma = 2$ nm.

spatial order due to interference of tight bridges between an increasing number of NPs locally “bonded”.

The PMF between two NPs is defined as the change in free energy of the entire system or reversible work to bring a pair of NPs to a specified separation in the PNC.⁴⁴ It also can be thought of an effective potential between a pair of NPs mediated by polymers and other NPs in the PNC. Mathematically, it is given by $\beta W_{nn}(r) = -\ln g_{nn}(r)$, and results are shown in Figure 5b. The oscillatory form reflects segmental-scale polymer-packing correlations in the dense melt. The depth of the PMF attractive minima grows with loading, but their spatial range decreases with loading. Overall, the PMF is essentially zero beyond a length scale below an intersurface NP separation of one NP diameter. However, one can see that for the highest loading PNC, the PMF has a weak, longer range tail reflecting the emergence of long-wavelength concentration fluctuations, as per Figure 4. Another interesting trend in the PMF, potentially relevant to dynamics, is the barriers that separate the local minima. Recall that these relate directly to the depth of the local minima in the real-space $g_{nn}(r)$ in the interstitial regions, as per Figure 5a. At a fixed interparticle separation, the barriers decrease significantly with loading. We interpret this as a consequence of the fact that at higher loading, a tagged NP will have multiple NP neighbors, which can all participate in cohesive bridging configurations, thereby lowering the free energy cost of separating NPs.

5.2. Coordination Numbers and Effective NP Radius.

Knowledge of the real-space NP–NP pair correlation function and PMF immediately allows two other interesting structural quantities to be computed. The first is the number of neighbors a tagged NP at the origin has as a continuous function of distance. This is calculated from integration of $g_{nn}(r)$ from $r = 0$ to the distance r of interest. Results are shown in Figure 6a. The step-like behavior reflects the well-defined interstitial spaces in the bridging-controlled packing correlations discussed above. At a surface-to-surface separation of two polymer segments, the NP coordination numbers increase from $\ll 1$ to ~ 1 to ~ 4 as NP packing fraction grows from 0.06 to 0.16 to 0.27, respectively. At the next neighbor level (three segments between NP surfaces), the total coordination numbers are ~ 0.5 , ~ 2 , and ~ 6 . As demonstrated in Figure S7, it is these two separations that dominate the interfacial CED. Because a coordination number of roughly 2 is associated with bond percolation, our calculations suggest that percolation occurs at a NP loading of $\sim 16\%$. Interestingly, the latter is close to dynamic percolation thresholds deduced using rheology³⁵ for SiO_2 –P2VP PNCs with a NP diameter of $D \sim 15$ nm. The sensitivity of the results in Figure 6a to

temperature is almost negligible (not shown), as expected from Figure 4.

A second quantity of interest is an “effective NP radius”, deduced here from a liquid-state physics perspective for spherical particles that interact via soft repulsions.^{44,49} Specifically, adopting the PMF as an effective 2-particle pair potential, we compute the “distance of the closest approach” if NPs have a thermal-like energy of 1 or $2 k_B T$ (as per a classical turning point in a two-particle collision). The results are shown in Figure 6b as the magnitude of radius enhancement, h_b , defined as one-half of the computed distance of the closest approach. We find that h_b varies from roughly two to one segment diameters with increased loading. The reduction with NP loading is a natural consequence of the “adsorbed layers” being soft and penetrable.

6. INTERFACIAL AND POLYMER STRUCTURE AND PROPERTIES

We now present PRISM theory predictions for the real-space polymer–NP interfacial correlations and CED and polymer correlations in real and Fourier space.

6.1. Interfacial Packing and Cohesion. Figure 7 shows the interfacial segment NP site–site pair correlation functions. The very high contact values reflect the strong adsorption of segments on NP surfaces. However, the contact peak decreases with loading, with values of 38.8, 36.5, 31.3, and 25.4 predicted for NP packing fractions of 0.01, 0.06, 0.16, and 0.27,

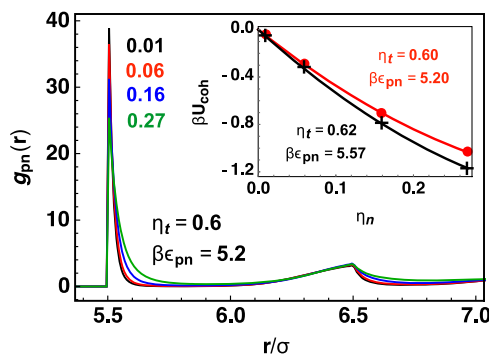


Figure 7. Polymer–NP site–site pair correlation function as a function of reduced separation for different loadings. The contact values are 38.8, 36.5, 31.3, and 25.4 with increasing loading. Inset: loading dependence of the CED in thermal energy units as a function of NP loading for two sets of η_t and $\beta\epsilon_{pn}$ values relevant to the experimental PNC at 180 and 150 °C. Lines are fit to the formula $A\eta_n(1 - \eta_n)$.

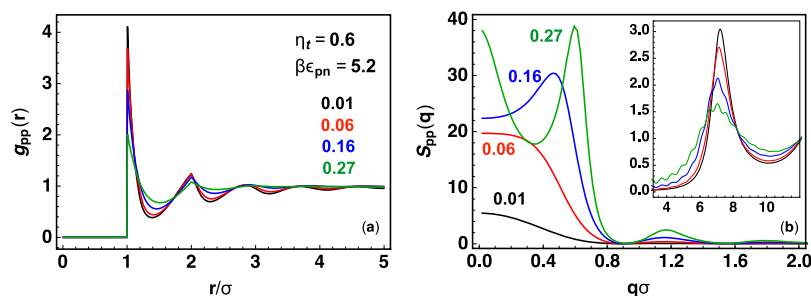


Figure 8. (a) Segment–segment pair correlation function as a function of reduced separation and different loadings for $\eta_t = 0.60$ and $\beta\epsilon_{pn} = 5.2$. With increasing NP loading, the contact values decrease as 4.1, 3.7, 2.9, and 2.0. (b) Corresponding collective structure factors in the small-wavevector regime. Inset: an expanded view of the primary cage or amorphous halo region.

respectively. This significant reduction is a well-known interference effect²¹ that occurs because as more NPs are added and their intersurface separation decreases, polymer layering correlations around isolated particles overlap, resulting in a change in the spatially resolved polymer density near a NP surface. This is a general effect present regardless of the strength of the interfacial attraction, although it is quantitatively intensified in the strong bridging microstructural regime of Figure 1 relevant to our present experimental PNC. For example, at 27% loading, we find (not shown) that the contact value of $g_{pn}(r)$ is reduced relative to the dilute NP limit by a factor of ~ 1.5 , 1.63, and 1.92 for dimensionless effective interfacial attraction energies of 0.3, 1, and 5.2, respectively, which span the three microstructural organization regimes in Figure 1. We note that a decrease in the polymer density close to the NP surface with loading has been reported in several experimental studies.^{6,9} Although the manner in which the interfacial layer density was experimentally extracted precludes a precise comparison to our results in Figure 7, the theoretical calculations seem at least consistent with the idea that the observed density reduction is an equilibrium packing effect.

The inset of Figure 7 shows the PNC CED, the absolute value of which is defined as

$$U_{\text{coh}} = 4\pi\rho_n\rho_p \int_0^\infty dr r^2 g_{pn}(r) |u_{pn}(r)| \quad (6)$$

Because the bare attraction range is short, the CED is dominated by close contacts between segments and a NP surface. CED results are shown in the inset of Figure 7 for two temperatures. The curve through the data points is the simple stoichiometric factor in eq 6. Its excellent reproduction of the dependence of the CED on loading is surprising because the interfacial packing correlations are highly nonrandom. However, because CED is an integrated quantity, and because the interfacial $g_{pn}(r)$ has a very sharp peak and then goes below unity on small length scales, the loading dependence (but not the absolute magnitude) of the CED is nearly identical to what is obtained if the mean field or random choice of $g_{pn}(r) = 1$ is employed in eq 6.

6.2. Polymer Correlations and Small- and Wide-Angle Scattering Patterns. Figure 8a presents calculations of the polymer segment–segment pair correlation functions in real space. All pairs of segments on different polymer chains contribute, including those *not* in cohesive contact with the NP and those that are. The net effect of adding NPs is to reduce the local caging correlations, as reflected in a decrease in the contact peak by a factor of ~ 2 at the highest NP loading and a decrease in both the amplitude and spatial range of oscillations

(density correlation length) associated with polymer solvation shells. One can view this as a generic packing frustration effect due to the fact that segments have to optimally pack (minimize free energy) in a way consistent not only with excluded volume constraints between themselves as in a pure melt, but also with excluded volume repulsions and interfacial cohesive attractions with the NPs. We find (not shown) that the change with loading of the p–p contact value relative to its pure melt value depends weakly on interfacial attraction strength, although the effect is perturbatively larger when there is strong bridging.

Figure 8b shows the analogous Fourier space polymer collective partial structure factors. As discussed in depth previously,^{21,34} the main frame shows a transition in the small q regime with loading from monotonic decay to nonmonotonic behavior with a finite wavevector “microphase-like” peak. The latter occurs at a wavevector that scales as the inverse NP diameter and shifts to smaller scales as loading grows. This microphase-like peak is a well-known generic “templating” effect associated mainly with the exclusion of polymers from the interior of spatially correlated NPs, and also the change in polymer packing in layers near a NP surface. Prior SAXS and small-angle neutron scattering experiments^{32,34} have observed this feature in different PNCs, which always narrows and becomes more intense as loading grows. In contrast, the scattering amplitude at $q \rightarrow 0$ monotonically increases with loading, reflecting in part the approach to a spinodal demixing boundary associated with bridging network formation.

The inset of Figure 8b shows an expanded view of the polymer amorphous halo or cage feature associated with local segmental packing correlations. This peak monotonically decreases in amplitude and broadens with NP loading because of the packing frustration effect discussed above. This is a large effect because a change in a caging peak by a factor of 2 is highly nonperturbative. In contrast, there is only a mild shift of the cage peak position toward lower $q\sigma$ (by a tiny amount of ~ 0.2) as NP loading increases. New wide-angle scattering experiments may potentially be able to probe this behavior.

7. SUMMARY AND DISCUSSION

We have performed SAXS measurements to study the evolution of length-scale-dependent NP correlations over a wide range of particle loadings in miscible silica–P2VP nanocomposites characterized by strong interfacial attraction. The cage peak associated with spatial correlations on the NP size scale evolves in a commonly observed manner with increasing NP concentration, as does the intermediate length scale amplitude of the structure factors. However, for wavevectors that probe long-wavelength NP concentration

fluctuations, a complex behavior is observed, with the higher loading PNCs showing a nonmonotonic change with wavevector because of an upturn of the structure factor on the longest length scales. The latter behavior results in the crossing of the 16 and 27% NP-loading structure factor curves. These trends suggest that the PNC is approaching a spinodal demixing transition. Given the strong interfacial attraction, prior theoretical PRISM theory work has predicted that its nature involves a polymer bridging-induced network type of demixing. This interpretation is buttressed by our TEM images which show a strongly heterogeneous NP microstructure on relatively local scales. This overall behavior is nearly independent of temperature over the limited range studied.

PRISM theory was applied in its minimalist model form where there is only one effective interfacial attraction energy. Variation in this chemically-specific number and the total mixture packing fraction over sensible ranges results in a good description of the key features of the SAXS data, especially on intermediate and long length scales. Because PRISM theory predicts that the low wavevector features arise from small-scale bridging effects, the theory–experiment agreement supports the conclusion that a network-like phase separation occurs in this PNC.

The theory with validated parameters was then used to make predictions for the real-space pair correlation functions between all species, small and large wavevector polymer collective structure factors, spatially-resolved NP coordination numbers, the interfacial CED, and an effective NP particle radius deduced from the 2-particle PMF. Intensification of small length scale bridging-induced configurations of NPs with increasing loading is predicted, while interpolymer and polymer–NP packing correlations weaken as more NPs are added to the melt. The latter is reflected in the polymer collective structure factor which exhibits a cage peak that is strongly reduced with loading because of packing frustration effects. This local reorganization of the polymer structure coexists with macro- and microphase separation features at low wavevectors which vary distinctively with NP loading.

Finally, the present work sets the stage for studying collective NP dynamics. Modern theoretical approaches require as input the equilibrium collective structure factors, and our results will provide such foundational information. A combined XPCS and dynamical theory study of $S_{nn}(q, t)$ is underway and will be reported in a future publication.

■ ASSOCIATED CONTENT

SI Supporting Information

The Supporting Information is available free of charge at <https://pubs.acs.org/doi/10.1021/acs.macromol.0c01391>.

Raw SAXS intensity data and experimental $S_{nn}(q)$ at 150 °C. Theoretical calculations of NP-scattering structure factors using the adjusted packing fraction and effective hard-sphere models, and also of the interfacial cohesive energy density. Direct comparison of theory versus experimental data for the NP scattering functions (PDF)

■ AUTHOR INFORMATION

Corresponding Author

Kenneth S. Schweizer – Department Materials Science and Engineering, Materials Research Laboratory, and Department of Chemistry, University of Illinois, Urbana, Illinois 61801, United States; Email: kschweiz@illinois.edu

Authors

Yuxing Zhou – Department Materials Science and Engineering and Materials Research Laboratory, University of Illinois, Urbana, Illinois 61801, United States; orcid.org/0000-0002-4476-0680

Benjamin M. Yavitt – Department of Materials Science and Chemical Engineering, Stony Brook University, Stony Brook, New York 11794, United States; orcid.org/0000-0001-9308-7472

Zhengping Zhou – Chemical Sciences Division, Oak Ridge National Laboratory, Oak Ridge, Tennessee 37831, United States

Vera Bocharova – Chemical Sciences Division, Oak Ridge National Laboratory, Oak Ridge, Tennessee 37831, United States; orcid.org/0000-0003-4270-3866

Daniel Salatto – Department of Materials Science and Chemical Engineering, Stony Brook University, Stony Brook, New York 11794, United States

Maya K. Endoh – Department of Materials Science and Chemical Engineering, Stony Brook University, Stony Brook, New York 11794, United States; orcid.org/0000-0001-6473-5047

Alexander E. Ribbe – Department for Polymer Science & Engineering, University of Massachusetts, Amherst, Massachusetts 01003, United States; orcid.org/0000-0002-9924-3429

Alexei P. Sokolov – Chemical Sciences Division, Oak Ridge National Laboratory, Oak Ridge, Tennessee 37831, United States; Department of Chemistry, University of Tennessee, Knoxville, Tennessee 37996, United States; orcid.org/0000-0002-8187-9445

Tadanori Koga – Department of Materials Science and Chemical Engineering, Stony Brook University, Stony Brook, New York 11794, United States; orcid.org/0000-0003-1316-6133

Complete contact information is available at:

<https://pubs.acs.org/doi/10.1021/acs.macromol.0c01391>

Notes

The authors declare no competing financial interest.

■ ACKNOWLEDGMENTS

Work at Illinois (Y.Z., K.S.S.) and ORNL (Z.Z., V.B., A.P.S.) was supported by the U.S. Department of Energy, Office of Science, Basic Energy Sciences, Materials Sciences and Engineering Division. T.K. acknowledges financial support for work at SBU from Henkel Corporation and Brookhaven National Laboratory. Acknowledgment is made to the Donors of the American Chemical Society Petroleum Research Fund for partial support of this research (T.K.). This research used resources of the Complex Materials Scattering (CMS/11-BM) beam line, operated by the National Synchrotron Light Source II, which are U.S. DOE Office of Science Facilities, at Brookhaven National Laboratory under Contract DE-SC0012704. The authors thank Ruipeng Li and Masafumi Fukuto at NSLS-II for their help performing the SAXS experiments.

■ REFERENCES

(1) Crosby, A. J.; Lee, J. Y. Polymer Nanocomposites: The “Nano” Effect on Mechanical Properties. *Polym. Rev.* **2007**, *47*, 217–229.

- (2) Kumar, S. K.; Benicewicz, B. C.; Vaia, R. A.; Winey, K. I. 50th Anniversary Perspective: Are Polymer Nanocomposites Practical for Applications? *Macromolecules* **2017**, *50*, 714–731.
- (3) Bailey, E. J.; Winey, K. I. Dynamics of Polymer Segments, Polymer Chains, and Nanoparticles in Polymer Nanocomposite Melts: A Review. *Prog. Polym. Sci.* **2020**, *105*, 101242.
- (4) Gam, S.; Meth, J. S.; Zane, S. G.; Chi, C.; Wood, B. A.; Winey, K. I.; Clarke, N.; Composto, R. J. Polymer Diffusion in a Polymer Nanocomposite: Effect of Nanoparticle Size and Polydispersity. *Soft Matter* **2012**, *8*, 6510–6512.
- (5) Bailey, E. J.; Griffin, P. J.; Composto, R. J.; Winey, K. I. Multiscale Dynamics of Small, Attractive Nanoparticles and Entangled Polymers in Polymer Nanocomposites. *Macromolecules* **2019**, *52*, 2181–2188.
- (6) Genix, A.-C.; Bocharova, V.; Carroll, B.; Lehmann, M.; Saito, T.; Krueger, S.; He, L.; Dieudonné-George, P.; Sokolov, A. P.; Oberdisse, J. Understanding the Static Interfacial Polymer Layer by Exploring the Dispersion States of Nanocomposites. *ACS Appl. Mater. Interfaces* **2019**, *11*, 17863–17872.
- (7) Jouault, N.; Moll, J. F.; Meng, D.; Windsor, K.; Ramcharan, S.; Kearney, C.; Kumar, S. K. Bound Polymer Layer in Nanocomposites. *ACS Macro Lett.* **2013**, *2*, 371–374.
- (8) Krutyeva, M.; Wischniewski, A.; Monkenbusch, M.; Willner, L.; Maiz, J.; Mijangos, C.; Arbe, A.; Colmenero, J.; Radulescu, A.; Holderer, O.; Ohl, M.; Richter, D. Effect of Nanoconfinement on Polymer Dynamics: Surface Layers and Interphases. *Phys. Rev. Lett.* **2013**, *110*, 108303.
- (9) Cheng, S.; Holt, A. P.; Wang, H.; Fan, F.; Bocharova, V.; Martin, H.; Etampawala, T.; White, B. T.; Saito, T.; Kang, N.-G.; Dadmun, M. D.; Mays, J. W.; Sokolov, A. P. Unexpected Molecular Weight Effect in Polymer Nanocomposites. *Phys. Rev. Lett.* **2016**, *116*, 038302.
- (10) Holt, A. P.; Griffin, P. J.; Bocharova, V.; Agapov, A. L.; Imel, A. E.; Dadmun, M. D.; Sangoro, J. R.; Sokolov, A. P. Dynamics at the Polymer/Nanoparticle Interface in Poly(2-Vinylpyridine)/Silica Nanocomposites. *Macromolecules* **2014**, *47*, 1837–1843.
- (11) Papon, A.; Montes, H.; Hanafi, M.; Lequeux, F.; Guy, L.; Saalwächter, K. Glass-Transition Temperature Gradient in Nanocomposites: Evidence from Nuclear Magnetic Resonance and Differential Scanning Calorimetry. *Phys. Rev. Lett.* **2012**, *108*, 065702.
- (12) Mortazavian, H.; Fennell, C. J.; Blum, F. D. Structure of the Interfacial Region in Adsorbed Poly(Vinyl Acetate) on Silica. *Macromolecules* **2016**, *49*, 298–307.
- (13) Mujtaba, A.; Keller, M.; Ilisch, S.; Radosch, H.-J.; Beiner, M.; Thurn-Albrecht, T.; Saalwächter, K. Detection of Surface-Immobilized Components and Their Role in Viscoelastic Reinforcement of Rubber-Silica Nanocomposites. *ACS Macro Lett.* **2014**, *3*, 481–485.
- (14) Roh, J. H.; Tyagi, M.; Hogan, T. E.; Roland, C. M. Effect of Binding to Carbon Black on the Dynamics of 1,4-Polybutadiene. *J. Chem. Phys.* **2013**, *139*, 134905.
- (15) Bailey, E. J.; Griffin, P. J.; Tyagi, M.; Winey, K. I. Segmental Diffusion in Attractive Polymer Nanocomposites: A Quasi-Elastic Neutron Scattering Study. *Macromolecules* **2019**, *52*, 669–678.
- (16) Ciprari, D.; Jacob, K.; Tannenbaum, R. Characterization of Polymer Nanocomposite Interphase and Its Impact on Mechanical Properties. *Macromolecules* **2006**, *39*, 6565–6573.
- (17) Meng, D.; Kumar, S. K.; Cheng, S.; Grest, G. S. Simulating the Miscibility of Nanoparticles and Polymer Melts. *Soft Matter* **2013**, *9*, 5417–5427.
- (18) Starr, F. W.; Douglas, J. F.; Meng, D.; Kumar, S. K. Bound Layers “Cloak” Nanoparticles in Strongly Interacting Polymer Nanocomposites. *ACS Nano* **2016**, *10*, 10960–10965.
- (19) Molinari, N.; Sutton, A. P.; Mostofi, A. A. Mechanisms of Reinforcement in Polymer Nanocomposites. *Phys. Chem. Chem. Phys.* **2018**, *20*, 23085–23094.
- (20) Hooper, J. B.; Schweizer, K. S. Theory of Phase Separation in Polymer Nanocomposites. *Macromolecules* **2006**, *39*, 5133–5142.
- (21) Hall, L. M.; Schweizer, K. S. Many Body Effects on the Phase Separation and Structure of Dense Polymer-Particle Melts. *J. Chem. Phys.* **2008**, *128*, 234901–234916.
- (22) Starr, F. W.; Douglas, J. F. Modifying Fragility and Collective Motion in Polymer Melts with Nanoparticles. *Phys. Rev. Lett.* **2011**, *106*, 115702–115704.
- (23) Liu, J.; Gao, Y.; Cao, D.; Zhang, L.; Guo, Z. Nanoparticle Dispersion and Aggregation in Polymer Nanocomposites: Insights from Molecular Dynamics Simulation. *Langmuir* **2011**, *27*, 7926–7933.
- (24) Starr, F. W.; Douglas, J. F.; Glotzer, S. C. Origin of Particle Clustering in a Simulated Polymer Nanocomposite and Its Impact on Rheology. *J. Chem. Phys.* **2003**, *119*, 1777–1788.
- (25) Ganesan, V.; Jayaraman, A. Theory and Simulation Studies of Effective Interactions, Phase Behavior and Morphology in Polymer Nanocomposites. *Soft Matter* **2014**, *10*, 13–38.
- (26) Li, Y.; Kröger, M.; Liu, W. K. Nanoparticle Effect on the Dynamics of Polymer Chains and Their Entanglement Network. *Phys. Rev. Lett.* **2012**, *109*, 118001.
- (27) Hooper, J. B.; Schweizer, K. S.; Desai, T. G.; Koshy, R.; Koblinski, P. Structure, Surface Excess and Effective Interactions in Polymer Nanocomposite Melts and Concentrated Solutions. *J. Chem. Phys.* **2004**, *121*, 6986–6997.
- (28) Martin, T. B.; Gartner, T. E.; Jones, R. L.; Snyder, C. R.; Jayaraman, A. PyPRISM: A Computational Tool for Liquid-State Theory Calculations of Macromolecular Materials. *Macromolecules* **2018**, *51*, 2906–2922.
- (29) Modica, K. J.; Martin, T. B.; Jayaraman, A. Effect of Polymer Architecture on the Structure and Interactions of Polymer Grafted Particles: Theory and Simulations. *Macromolecules* **2017**, *50*, 4854–4866.
- (30) Gucht, J. v. d.; Spruijt, E.; Lemmers, M.; Cohen Stuart, M. A. Polyelectrolyte Complexes: Bulk Phases and Colloidal Systems. *J. Colloid Interface Sci.* **2011**, *361*, 407–422.
- (31) Liu, X.; Chapel, J.-P.; Schatz, C. Structure, Thermodynamic and Kinetic Signatures of a Synthetic Polyelectrolyte Coacervating System. *Adv. Colloid Interface Sci.* **2017**, *239*, 178–186.
- (32) Hall, L. M.; Anderson, B. J.; Zukoski, C. F.; Schweizer, K. S. Concentration Fluctuations, Local Order, and the Collective Structure of Polymer Nanocomposites. *Macromolecules* **2009**, *42*, 8435–8442.
- (33) Kim, S. Y.; Hall, L. M.; Schweizer, K. S.; Zukoski, C. F. Long Wavelength Concentration Fluctuations and Cage Scale Ordering of Nanoparticles in Concentrated Polymer Solutions. *Macromolecules* **2010**, *43*, 10123–10131.
- (34) Kim, S. Y.; Schweizer, K. S.; Zukoski, C. F. Multiscale Structure, Interfacial Cohesion, Adsorbed Layers, and Thermodynamics in Dense Polymer-Nanoparticle Mixtures. *Phys. Rev. Lett.* **2011**, *107*, 225504.
- (35) Chen, Q.; Gong, S.; Moll, J.; Zhao, D.; Kumar, S. K.; Colby, R. H. Mechanical Reinforcement of Polymer Nanocomposites from Percolation of a Nanoparticle Network. *ACS Macro Lett.* **2015**, *4*, 398–402.
- (36) Iijima, M.; Kamiya, H. Layer-by-Layer Surface Modification of Functional Nanoparticles for Dispersion in Organic Solvents. *Langmuir* **2010**, *26*, 17943–17948.
- (37) Kamiya, H.; Suzuki, H.; Kato, D.; Jimbo, G. Densification of Alkoxide-Derived Fine Silica Powder Compact by Ultra-High-Pressure Cold Isostatic Pressing. *J. Am. Ceram. Soc.* **1993**, *76*, 54–64.
- (38) Genix, A.-C.; Bocharova, V.; Kisliuk, A.; Carroll, B.; Zhao, S.; Oberdisse, J.; Sokolov, A. P. Enhancing the Mechanical Properties of Glassy Nanocomposites by Tuning Polymer Molecular Weight. *ACS Appl. Mater. Interfaces* **2018**, *10*, 33601–33610.
- (39) Baeza, G. P.; Dessi, C.; Costanzo, S.; Zhao, D.; Gong, S.; Alegria, A.; Colby, R. H.; Rubinstein, M.; Vlassopoulos, D.; Kumar, S. K. Network Dynamics in Nanofilled Polymers. *Nat. Commun.* **2016**, *7*, 11368.
- (40) van Zanten, J. H.; Wallace, W. E.; Wu, W.-I. Effect of Strongly Favorable Substrate Interactions on the Thermal Properties of Ultrathin Polymer Films. *Phys. Rev. E: Stat. Phys., Plasmas, Fluids, Relat. Interdiscip. Top.* **1996**, *53*, R2053–R2056.

- (41) Gong, S.; Chen, Q.; Moll, J. F.; Kumar, S. K.; Colby, R. H. Segmental Dynamics of Polymer Melts with Spherical Nanoparticles. *ACS Macro Lett.* **2014**, *3*, 773–777.
- (42) Kline, S. R. Reduction and Analysis of SANS and USANS Data Using IGOR Pro. *J. Appl. Crystallogr.* **2006**, *39*, 895–900.
- (43) Honnell, K. G.; Curro, J. G.; Schweizer, K. S. Local Structure of Semiflexible Polymer Melts. *Macromolecules* **1990**, *23*, 3496–3505.
- (44) Hooper, J. B.; Schweizer, K. S. Contact Aggregation, Bridging, and Steric Stabilization in Dense Polymer-Particle Mixtures. *Macromolecules* **2005**, *38*, 8858–8869.
- (45) Schweizer, K. S.; Curro, J. G. Integral Equation Theory of Polymer Melts: Intramolecular Structure, Local Order, and the Correlation Hole. *Macromolecules* **1988**, *21*, 3070–3081.
- (46) Curro, J. G.; Schweizer, K. S.; Grest, G. S.; Kremer, K. A Comparison between Integral Equation Theory and Molecular Dynamics Simulations of Dense, Flexible Polymer Liquids. *J. Chem. Phys.* **1989**, *91*, 1357–1364.
- (47) Kinoshita, M. Interaction between Surfaces with Solvophobicity or Solvophilicity Immersed in Solvent: Effects Due to Addition of Solvophobic or Solvophilic Solute. *J. Chem. Phys.* **2003**, *118*, 8969–8981.
- (48) Zhou, Y.; Schweizer, K. S. Local Structure, Thermodynamics, and Phase Behavior of Asymmetric Particle Mixtures: Comparison between Integral Equation Theories and Simulation. *J. Chem. Phys.* **2019**, *150*, 214902–214912.
- (49) Speedy, R. J.; Prielmeier, F. X.; Vardag, T.; Lang, E. W.; Lüdemann, H.-D. Diffusion in Simple Fluids. *Mol. Phys.* **1989**, *66*, 577–590.